Novel acid-free process intensification for the synthesis of non-precious metal-nitrogen-carbon electrocatalysts for oxygen reduction reaction

Original
Novel acid-free process intensification for the synthesis of non-precious metal-nitrogen-carbon electrocatalysts for oxygen reduction reaction / Cosenza, A.; Delafontaine, L.; Ly, A.; Wang, H.; Murphy, E.; Liu, Y.; Specchia, S.; Atanassov, P.. - In: JOURNAL OF POWER SOURCES. - ISSN 0378-7753. - STAMPA. - 556:(2023), pp. 1-10. [10.1016/j.jpowsour.2022.232382]

Availability:
This version is available at: 11583/2973896 since: 2022-12-16T07:52:56Z

Publisher:
Elsevier B.V.

Published
DOI:10.1016/j.jpowsour.2022.232382

Novel acid-free process intensification for the synthesis of non-precious metal-nitrogen-carbon electrocatalysts for oxygen reduction reaction

†Alessio Cosenza[a,1], †Laurent Delafontaine[a], Alvin Ly[a], Hanson Wang[a], Eamonn Murphy[a], Yuanchao Liu[a], Stefania Specchia[1] and Plamen Atanassov[a,b,*]

[a]Department of Chemical and Biomolecular Engineering, National Fuel Cell Research Center, University of California, Irvine, California 92697, USA

[b]Department of Materials Science and Engineering, University of California, Irvine, California 92697, USA

[1]Department of Applied Science and Technology, Politecnico di Torino, Corso Duca degli Abruzzi 24, 10129, Torino, Italy

*Corresponding author: plamen.atanassov@uci.edu (Plamen Atanassov)

†These authors contributed equally

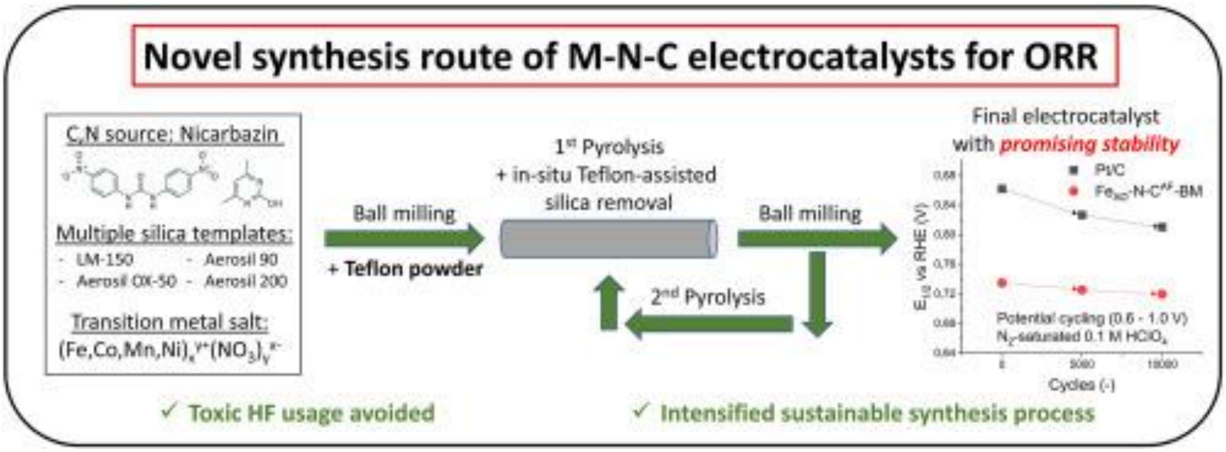

Abstract

In this work, a set of PGM-free mono-metallic electrocatalysts (Fe_{AD}-N-C^{AF}, Co-N-C^{AF}, Mn-N-C^{AF}, Ni-N-C^{AF}) were synthesized using multiple silica templates with a modified acid-free sacrificial support method, characterized and tested for oxygen reduction reaction (ORR) in acidic, neutral and alkaline electrolytes. The removal of the silica template is achieved simultaneously to pyrolysis through the addition of Teflon powder to the mass of precursors before the heat treatment, resulting in a simple, fast and green approach compared to the conventional method based on the use of hydrofluoric acid (HF). Rotating ring disk electrode tests show that the iron-based electrocatalyst, among all, have higher activity for ORR. An electrocatalyst loading study was conducted with Fe_{AD}-N-C^{AF} revealing a dual-site reaction mechanism and a maximum activity reached at 700 µg cm^{-2}, while accelerated durability test highlights its promising stability. This novel synthesis route can be classified as a new intensified sustainable synthesis process.

Keywords: M-N-C electrocatalysts; oxygen reduction; sustainable synthesis; process intensification; Teflon powder; PEMFC.

1. Introduction

Climate change is one of the crucial problems of the XXI century, with devastating effects on weather patterns, ecosystems, societies and economies [1]. Greenhouse gases are the main responsible and, among them, carbon dioxide gives the major contribution. CO_2 concentration in the atmosphere reached a value of 414 ppm in 2020 with an increment of about 50% respect to the pre-industrial level of 280 ppm, which remained constant for the previous 10000 years of Holocene with negligible variations. The Intergovernmental Panel on Climate Change (IPCC) states that the principal cause of the increasing CO_2 concentration is combustion of fossil fuels and deforestation, with sea level rise and acid rains as consequences [2]. In this context, the transition towards an emission-free way of producing energy is of vital importance and systems such as polymer electrolyte membrane fuel cells (PEMFCs) and metal-air batteries (MABs). However, the cathodic electrochemical reaction involved, oxygen reduction reaction (ORR), is sluggish and the required state-of-the-art electrocatalyst, platinum [3], is expensive, scarce and characterized by price volatility [4].

ORR mechanism in aqueous solutions involves several elementary steps and can occur through a direct four-electron pathway ($4e^-$ transfer) with reduction of O_2 to H_2O or through a two-electron pathway ($2e^-$ transfer) with formation of H_2O_2. Hydrogen peroxide can be further reduced leading to the flow of two additional electrons ($2x2e^-$ transfer) [5]. The direct total reduction is more efficient and does not involve the production of H_2O_2, a reactive and corrosive compound that can have a negative impact on the electrocatalyst durability [6].

Non-precious transition metal-nitrogen-carbon (M-N-C) electrocatalysts are the most promising alternative to platinum-based materials for ORR. Carbon has the purpose of conducting electrons and providing high surface area with a porous structure, transition metal is the heart of the electrocatalytic site as a single atom and nitrogen is able to coordinate the transition metal atom linking it to the carbonaceous structure [7].

From an historical point of view, the development of those materials started around 1960 when it was discovered that cobalt phthalocyanine is active towards ORR [8]. It is a macrocyclic organic compound with four nitrogen atoms coordinating a single cobalt atom. Since those molecules lack of durability in acid environment, it was found that heat treatment at high temperature (400-1000 °C) can be an effective way to increase both their stability and activity. Later it was shown that atomically dispersed active sites can be obtained through pyrolysis from every source of carbon and nitrogen atoms in the presence of transition metal salts [9].

Those electrocatalysts show a plurality of possible active sites, depending on how the transition metal is coordinated by nitrogen atoms. Generally, they are located as defects on graphitic planes and their general formula is M-N_x, where x represents the number of nitrogen atoms coordinating the metal atom. Several types of coordination are possible and each of them show a different binding energy to the reactant with consequent different activity [10,11]. M-N_4 site is believed to be the main electrocatalytic site for ORR showing an optimal binding energy [12,13]. Metal-free N-C moieties that are present in those materials are also believed to contribute to the electrocatalytic activity; in particular, an increasing content of pyridinic nitrogen is beneficial for ORR and graphitic nitrogen can facilitate the adsorption of oxygen molecules [12,14,15].

There are different approaches for the synthesis of those electrocatalysts that share some aspects in common, such as mixing of precursors, pyrolysis and acid washing [16,17]. Compounds with high N:C atomic ratio such as nicarbazin and melamine are desirable in order to incorporate the highest possible number of nitrogen atoms in the carbon structure increasing the density of active sites. Pyrolysis is the key to obtain the final structure of the electrocatalyst with atomically dispersed active sites, since it provides the energy to recombine the chemical bonds. It is a thermochemical decomposition of reactants in anoxic conditions where temperatures in the range 700-1100 °C are necessary to decompose the carbon source. Variables such as the ramp rate, final temperature and gas composition can be optimized to finely tune the final structure of the material [18]; in particular, some previous works show how a ramp rate of about 10 °C min^{-1} allows to maximize the pore volume while the final temperature must be accurately selected in order to avoid agglomeration of metal particles and excessive graphitization [19]. The presence of ammonia in the pyrolysis atmosphere leads to an increased activity since it results in a greater specific surface area respect to the use of inert gases, although it does not influence the nature of nitrogen moieties and the entity of nitrogen doping [20]. Acid washing is the successive step for the removal of acid soluble metal containing compounds such as metal/metal oxide nanoparticles that are not strongly bonded to the carbon structure. Since they do not contribute to the electrocatalytic activity, they represent an inert mass that is generally removed through HCl or H_2SO_4 acid solutions [21,22]. Finally a second pyrolysis step is important since it can improve the morphology of the porous structure and the configuration of nitrogen, boosting the electrocatalytic activity [23].

In this work the focus is on the sacrificial support method (SSM), developed by Atanassov's group at University of New Mexico [24], based on the mixing of silica particles together with the precursors through ball milling, solvent evaporation or wet impregnation before pyrolysis [25–27]. This approach allows to negatively replicate the tridimensional porous structure of silica and to obtain an electrocatalyst with controlled porosity and atomically dispersed active sites [28]. Finally, a treatment with HF aqueous solution (5-25 wt. %) or alkaline KOH aqueous solution is necessary for the removal of the silica template maintaining at the same time the morphology of the electrocatalyst [29]. Increasing the amount of metal salt does not allow to atomically disperse all the transition metal atoms since there is a limit amount that can be incorporated as single atoms, this is why the masses of precursors are other variables to be optimized [30]. This method is the only one that has been developed in the industrial world by Pajarito Powder company for the synthesis of non-noble metal electrocatalysts, since it allows to achieve both stability and activity [31]. However, there are some problems to be solved such as the huge amount of liquid acid waste that is produced (HF aqueous solution), that requires downstream processes for its treatment and represents a danger for human beings and environment placing question marks on the sustainability of the whole process.

This study explores for the first time a sustainable and environmentally friendly variation of the traditional sacrificial support method, based on the addition of Teflon powder to the mass of precursors before pyrolysis without further acid washing. In such a way, the use of HF is totally avoided, with increased safety for the operators and more respect for the environment. The idea comes from previous works in the fields of supercapacitors and carbon capture for the synthesis of carbonaceous porous structures based on the use of silica templates [32–34]. The use of polytetrafluoroethylene allowed to achieve carbon materials with strongly enhanced surface area and higher microporosity, leading to a complete removal of silica during heat treatment through in situ decomposition of Teflon with chain mechanism and consequent in situ formation of minimal amount of gaseous HF, that is able to rapidly react with silicon producing gaseous silicon tetrafluoride (SiF_4). In such a way, emissions of harmful HF are completely avoided [33]. The PTFE/silicon mass ratio and pyrolysis time are key variables to determine the final morphology of the material. In particular, reducing the amount of Teflon at constant mass of silica and increasing pyrolysis time the surface area and pore volume are decreased [33]. This approach allows to drastically reduce the synthesis time since no further steps of acid washing are necessary and to avoid simultaneously the treatment of huge amounts of liquid waste. Thus, this new synthesis approach can be defined green and sustainable, and can be classified under the umbrella of “process intensification” (PI). By definition, in fact, PI observes the conceptual design principles for a safe chemical process according to an inherent safety process (safety-by-design) which i. avoids the use of extra chemicals or solvents; ii. avoids extra pumps or vessels; iii. reduces holdups and number of unit of operations; iv. refers to a inherent continuous process control [35,36].

Four mono-metallic electrocatalysts (Fe_{AD}-N-C^{AF}, Co-N-C^{AF}, Mn-N-C^{AF}, Ni-N-C^{AF}) were synthesized through modified sacrificial support method with the addition of Teflon powder to the mass of precursors before pyrolysis, characterized by physical-chemical methods (SEM, XPS, Raman Spectroscopy, XRD, STEM/EDS and BET) and tested for ORR in acidic, neutral and alkaline electrolytes. Nicarbazin was selected as the source of carbon and nitrogen atoms, hydrated nitrate salts were used to simultaneously provide additional nitrogen and transition metal atoms. RRDE tests show that activities comparable to state-of-the-art non-precious electrocatalysts are achievable and further improvements are possible. In detail, halfwave potentials of 0.73 V vs RHE in 0.1 M $HClO_4$ and 0.81 V vs RHE in 0.1 M KOH were obtained through the iron-based material with $4e^-$ pathway for ORR and excellent stability. This study paves the road towards a novel and sustainable acid-free process for the synthesis of those materials which can be explored with different optimization routes.

2. Materials and methods

2.1 Chemicals

Nickel(II) nitrate hexahydrate (purity ≥ 98.5%), manganese(II) nitrate tetrahydrate (purity ≥ 97.0%), iron(III) nitrate nonahydrate (purity ≥ 98.0%), cobalt(II) nitrate hexahydrate (purity ≥ 98.0%), polytetrafluoroethylene powder (1 μm particle size), Nafion perfluorinated resin solution 5 wt. % and nicarbazin were purchased from Sigma-Aldrich (USA). LM-150 fumed silica (specific surface area ~150 m^2 g^{-1}) was purchased from Cabot (USA). Aerosil 90 (specific surface area ~90 m^2 g^{-1}) and Aerosil 200 (specific surface area ~200 m^2 g^{-1}) were purchased from Evonik (USA). Stöber's spheres (320 nm average diameter) were synthesized by Stöber's method [37]. Potassium hydroxide (purity ≥ 85.0%), sodium chloride (purity ≥ 99.5%), isopropanol (IPA, purity ≥ 99.9%), and hydrochloric acid (36.5 to 38 % m/w) were purchased from Fisher Chemical (USA). Perchloric acid 70% was purchased from Merck Millipore (USA) and ethyl alcohol was purchased from Gold Shield Distributors. Aluminum oxide polishing solution (5 μm) was purchased from Allied High Tech Products (USA). Nitrogen 6.0 was purchased from Linde (USA), oxygen 5.0 was purchased from Praxair (USA), and ammonia (9.9 mole %, nitrogen: balance) was purchased from Airgas (USA). Deionized ultrapure water (DIW) was obtained using a Millipore Milli-Q system (product water conductivity at 25 °C = 0.056 μS cm^{-1}).

2.2 Electrocatalyst synthesis

In the synthesis of Fe_{AD}-N-C^{AF}, Co-N-C^{AF}, Mn-N-C^{AF}, Ni-N-C^{AF} four different types of silica particles (Stöber’s spheres, Aerosil 90, Aerosil 200, LM-150 fumed silica) were simultaneously used for each electrocatalyst. The contemporaneous use of multiple varieties of silica with different surface area and porosity allows to obtain a hierarchical pore size distribution that is beneficial for the electrochemical reactions. In particular, the most active sites mainly sit in micropores, while mesopores facilitate the accessibility of gas or ions to the active sites and macropores enhance mass transport of reactants and products [6].

In the synthesis of the iron-based electrocatalyst, 6.25 g of nicarbazin, 1.19 g of iron nitrate nonahydrate, 1.25 g of LM-150 fumed silica, 0.5 g of Stöber’s spheres, 0.94 g of Aerosil 90 and 0.31 g of Aerosil 200 were dispersed in deionized water, sonicated for 30 min and mixed at 45 °C under constant stirring overnight (Cole-Parmer Stuart Stirring Hot Plate). To completely dry the precursors, a successive step in the oven at 60 °C and ambient pressure was realized. After grinding with mortar and pestle, a calculated amount of Teflon particles based on the wt. % of silica according to the following equation was added to the powder.

$$m_t(mg) = \frac{\left(mass\ of\ powder\ obtained\ after\ drying\ (mg)\right) * \frac{wt\ \%\ SiO_2}{100}}{\frac{0.09\ mg\ silica}{mg\ Teflon}} \qquad (1)$$

The mixture was then split equally in three agate ball mill jars (volume 100 ml each) with 32 agate balls (10 balls with 10.28 mm diameter, 22 balls with 6.26 mm diameter) in each jar and subject to ball-milling (PQ-N04 Planetary Ball Mill) at 10 Hz for 1 h. Since it was evident that Teflon powder tends to stick to the walls, every 15 min the jars were opened and the powder was mixed manually. The reactants were loaded into a weigh boat and subject to pyrolysis under 100 % N_2 atmosphere in a quartz tube, heating from room temperature to 900 °C with a ramp rate of 5 °C min^{-1} and a 180 min hold at 900 °C. A Thermcraft controller was used to regulate the temperature while MKS mass flow controller allowed to adjust the flow rate of nitrogen to 100 ml min^{-1}. The obtained powder was subject to ball-milling again at the same conditions described above and it is denoted as Fe-N-C-Postpyr1 in this study. Then, Fe-N-C-Postpyr1 was pyrolyzed for the second time under 9.9 mole % NH_3 and 90.1 mole % N_2 atmosphere with a ramp rate of 10 °C min^{-1} and 30 min hold at 950 °C to obtain Fe_{AD}-N-C^{AF}. A similar procedure was used to synthesize all the other materials and the mass proportions of the precursors are summarized in **Table 1**, where each raw is representative of an electrocatalyst and the amounts are normalized with respect to 1 g of hydrated nitrate salt. The mass ratios were selected so that each electrocatalyst shows the same amount of transition metal atoms per unit total mass of precursors, in order to be able to have a consistent comparison of performances.

Table 1. Precursors and mass ratios for the synthesis of M-N-C electrocatalysts.

SAMPLE	Me SOURCE	C,N SOURCE	SILICA TEMPLATE			
	Hydrated nitrate salt	Nicarbazin $C_{19}H_{18}N_6O_6$	LM-150 (SA ~ 150 m^2 g^{-1})	Stöber spheres	Aerosil 90 (SA ~ 90 m^2 g^{-1})	Aerosil 200 (SA ~ 200 m^2 g^{-1})
Fe_{AD}-N-C^{AF}	1 g $Fe(NO_3)_3 \cdot 9H_2O$	5.25 g	1.05 g	0.42 g	0.78 g	0.26 g
Ni-N-C^{AF}	1 g $Ni(NO_3)_2 \cdot 6H_2O$	7.26 g	1.45 g	0.58 g	1.09 g	0.36 g
Co-N-C^{AF}	1 g $Co(NO_3)_2 \cdot 6H_20$	7.26 g	1.45 g	0.58 g	1.09 g	0.36 g
Mn-N-C^{AF}	1 g	8.45 g	1.69 g	0.68 g	1.27 g	0.42 g

	$Mn(NO_3)_2 \cdot 4H_2O$					

A fraction of Fe_{AD}-N-C^{AF} total mass was also washed with hydrochloric acid aqueous solution at 80 °C for 8 h under constant stirring and centrifuged (Hermle Z366 centrifuge) through 6 cycles of 5 min each at 9200 rpm with intermediate deionized water rinsing between each cycle. The suspension was finally filtered under vacuum using a Buchner flask with a Nylon membrane (GVS Filter Technology, disk diam. 47 mm NY 0.22 μm) and washed with deionized water until the pH was neutral. The sample was then dried in the oven at ambient pressure and 55 °C overnight. The acid solution was prepared by mixing 4.35 ml of hydrochloric acid (36.5 to 38 % w/w) with 95.65 ml of deionized water. The notation used in this study for the acid-washed electrocatalyst is Fe-N-C-AW.

Another fraction of Fe_{AD}-N-C^{AF} powder was subject to a third ball-milling step at the same conditions described above and it is denoted as Fe_{AD}-N-C^{AF}-BM.

2.3 Physical-chemical characterization

Scanning electron microscopy (SEM) was conducted using a FEI Magellan 400 XHR SEM to visualize the surface morphology of the electrocatalysts. Current (50 pA – 0.80 nA) and voltage (18 kV - 20 kV) were adjusted for each electrocatalyst in order to focus and both TLD and ETD detectors were used depending on the case.

X-Ray photoelectron spectroscopy (XPS) on a Kratos AXIS Supra spectrometer with a monochromatic Al Kα source (1486.6 eV) at 15 mA anode current allowed to determine the atomic composition and chemical structure of the surface. Survey spectra were obtained in the range 0 to 1400 eV, detailed N_{1s} spectra in the range 390 to 415 eV, C_{1s} spectra in the range 270 to 300 eV and F_{1s} spectra in the range 675 to 695 eV. The calibration was performed respect to a value of the C_{1s} binding energy equal to 284.5 eV. To quantify the elemental composition Casa XPS is the software that was used, selecting a linear background for N 1s, C 1s, F 1s regions and a Shirley background for transition metal regions. Peak fitting was realized using a 70%/30% Gaussian/Lorentzian line shape.

X-ray diffraction (XRD) analysis was realized using a Rigaku Powder X-ray diffractometer with Cu (K radiation 0.15418 nm) run at 40 kV and 30 mA with a Nickel K-beta filter, a step size of 0.03° and 2θ varying from 20° to 85°, in order to understand the crystalline structure of the materials. Phase identification was conducted through the software PDXL and ICDD database.

Raman spectra were obtained through inVia, Renishaw Corp., UK system with a 633 nm laser to quantify the degree of disorder of carbon.

The morphology and single atom sites of the electrocatalyst was analyzed by aberration-corrected scanning transmission electron microscopy using a JOEL ARM-200F at an accelerating voltage of 200 kV.

The elemental distribution of the electrocatalyst was analyzed by energy dispersive X-Ray spectroscopy using a FEI Talos F200X at an accelerating voltage of 200 kV, equipped with superX 4 SSD EDX detectors.

N_2 physisorption was realized on a Micromeritics 3Flex Analyzer at a temperature of 77 K. The surface area and the distribution of the pore dimensions were calculated using the Brunauer-Emmett-Teller (BET) method and Barrett-Joyner-Halenda (BJH) method, respectively.

2.4 Electrochemical measurements

The electrochemical tests were conducted with a three electrode system (Pine research instrument), a potentiostat (BioLogic VSP-300), a rotating ring-disk electrode (Pine research instrument, glassy carbon disk 0.247 cm^2 geometric area, Pt ring), a rotation rate control unit (Pine research instrument), carbon rod as counter electrode, HydroFlex hydrogen reference electrode (Gaskatel) and a Teflon cell (200 ml).

Before any test, the working electrode and the ring were cleaned by wiping with ethanol and sonicating in ethanol for 10 minutes. Aluminum oxide (5 μm) solution was also used to polish the working electrode. The Teflon cell was cleaned by rinsing 5 times with deionized water at ambient temperature and by filling 1 time with deionized water bringing it to the boil through microwaves.

For ORR, the activity of the electrocatalysts was investigated in 0.1 M KOH (pH = 13), 0.1 M $HClO_4$ (pH = 1), 0.5 M NaCl (pH = 7) and 2 M NaCl (pH = 7) aqueous solutions saturated by bubbling O_2 or N_2. For each electrocatalyst the ink was prepared by mixing 3.94 mg of powder with 255.2 μl of DIW, 255.2 μl of IPA and 21.3 μl of Nafion perfluorinated resin solution 5 wt. %. Platinum on graphitized carbon (Pt/C, 20 wt. %) is used as a benchmark. The ink is based on 2.5 mg of Pt/C powder, 1619.4 μl of DIW, 1619.4 μl of IPA and 135.0 μl of Nafion perfluorinated resin solution 5 wt. %. The suspensions were then sonicated for 30 min at ambient temperature. 20 μl of ink were deposited onto the glassy carbon disk and dried at ambient conditions in such a way that electrocatalyst loadings of 600 μg cm^{-2} for PGM-free electrocatalysts and 60 μg cm^{-2} for Pt/C were obtained. The electrolytic solution was bubbled with N_2 for 15 min before any test in order to purge any other gas. Electrochemical impedance spectroscopy (EIS) was performed without rotation of the disk to evaluate the ohmic resistance of the solution, by setting the potential of the working electrode at 0.45 V vs RHE, the sinus amplitude at 10 mV and by varying the frequency in the range 1.0 Hz – 1.0 MHz. The solution resistance can be evaluated by extrapolating the real axis value at the high frequency intercept and it is useful for iR compensation. Prior to kinetic measurements, cyclic voltammetry (CV) in the potential range 0.05 – 1.23 V vs RHE with a scan rate of 500 mV s^{-1} was conducted for 100 cycles in order to activate and clean the surface of the electrocatalyst; this procedure was sufficient to obtain a stable response. Another CV under N_2 is collected at 1600 rpm at a scan rate of 5 mV s^{-1} in the potential window 0.1 – 1.05 V vs RHE to evaluate the capacitive current that was then removed from the current due to the electrocatalytic reaction. The electrolyte was saturated with O_2 for 15 min and a final CV at 1600 rpm was collected at a scan rate of 5 mV s^{-1} between 0.1 – 1.05 V vs RHE, fixing the potential of the ring at 1.1 V vs RHE to collect the current due to H_2O_2 oxidation. The anodic sweep was used to extract kinetic data. Each test was repeated twice.

The activity of the electrocatalysts towards ORR was evaluated by extracting from the anodic polarization curve the values of typical descriptors: the onset potential (E_{onset}) corresponding to a current density of 0.1 mA cm^{-2}, the halfwave potential ($E_{1/2}$) calculated through the first-derivative method [38], the number of electrons transferred (*n*) and the hydrogen peroxide yield (% H_2O_2) evaluated respectively with the following equations [39].

$$n = 4 * \frac{i_d}{i_d + \frac{i_r}{N}} \tag{2}$$

$$\%H_2O_2 = 2 * \frac{\frac{i_r}{N}}{i_d + \frac{i_r}{N}} \tag{3}$$

Where i_r and i_d are the absolute values of the ring current and the disk current respectively, while N is the collection efficiency of the ring which was empirically evaluated to be 0.5 through the reversible and single-electron ferrocyanide/ferricyanide half reaction.

An electrocatalyst loading study in the range 50 μg cm^{-2} – 900 μg cm^{-2} was conducted using Fe_{AD}-N-C^{AF}-BM electrocatalyst in 0.1 M $HClO_4$ electrolyte for ORR, by preparing inks at different concentrations and by executing RRDE tests at the same conditions described above; each test was repeated twice.

Accelerated durability testing was conducted on Fe_{AD}-N-C^{AF}-BM electrocatalyst with a loading of 700 μg cm^{-2} in N_2 saturated 0.1 M $HClO_4$ by cycling the potential between 0.60 and 1.00 V at 50 mV s^{-1}. The activity for ORR was evaluated through RRDE polarization curves at 1600 rpm in O_2 saturated electrolyte before and after 5,000 and 10,000 cycles.

3. Results and discussion

3.1 Structure and morphology

The crystalline structure of the materials was analyzed through XRD and the patterns are shown in **Fig. 1 a**. All the electrocatalysts show diffraction peaks at about 26° and 44° that can be both ascribed to graphitic carbon, respectively related to the (002) and (100) planes. The sharpness of the peak at 26° is decreasing following the order Ni-N-C^{AF} > Co-N-C^{AF} > Mn-N-C^{AF} > Fe_{AD}-N-C^{AF}, underlining that a different number of graphene layers is stacked in the carbonaceous structure among the different materials. This can be explained considering that the presence of transition metals can catalyze graphitization of carbon during heat treatment [40,41] and Ni demonstrate higher catalytic property in this sense. **Fig. S1 e-f** is an example of the catalytic graphitization property of Fe nanoparticles. Fe_{AD}-N-C^{AF} shows a broader peak at 26°, highlighting the presence of increased long-range disorder and lattice defects in the graphitic structure.

The presence of nanoparticles is evident for all the materials, as a consequence of agglomeration during the high-temperature pyrolysis. In detail, manganese carbide peaks (DB card number: 01-080-1701) at 44.2°, 51.4° and 75.8° respectively due to the (511), (600) and (660) diffraction planes are visible for the Mn-N-C^{AF} powder. Ni-N-C^{AF} sample shows narrow diffraction peaks at 44.5°, 51.8° and 76.4° which can be ascribed respectively to the (111), (200) and (220) planes of nickel (DB card number: 00-004-0850) and nickel carbide (DB card number: 01-074-5561) particles. It is evident from the sharpness of the reflections that Ni has a higher tendency to form bigger clusters and it is not homogeneously dispersed in the carbonaceous matrix. Fe_{AD}-N-C^{AF} peaks at 44.7° and 50.8° correspond to the (111) and (200) planes respectively of both iron (DB card number: 01-071-3739) and iron nitride (DB card number: 01-075-2127) clusters. However, the intensity associated to them is relatively lower demonstrating a more uniform dispersion of Fe in the tridimensional structure of the material. Co-N-C^{AF} pattern presents a variety of different peaks which qualitatively put under evidence different species such as cobalt carbide, cobalt nitride, cobalt oxide and cobalt particles.

No signals related to silicon dioxide are present, demonstrating a successful removal of the silica templates.

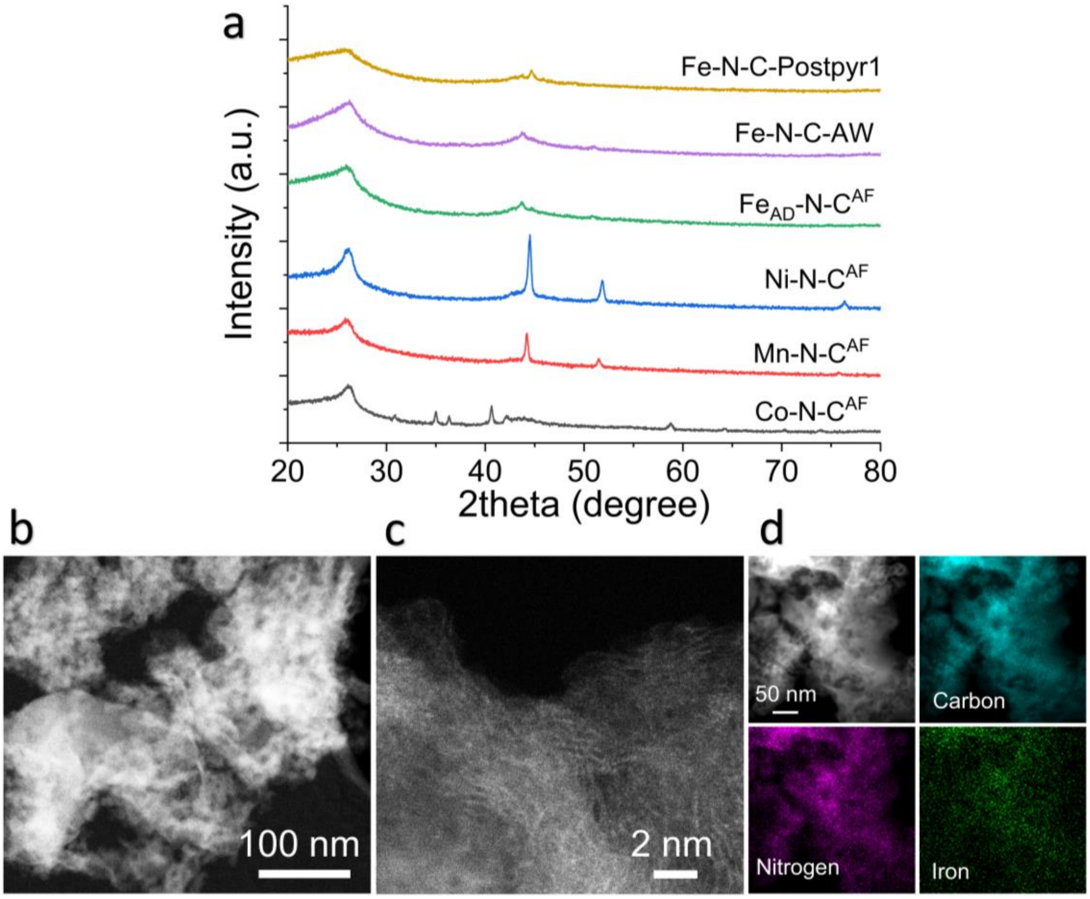

Figure 1. Chemical-physical characterization. (a) XRD patterns of Co-N-C^{AF}, Mn-N-C^{AF}, Ni-N-C^{AF}, Fe$_{AD}$-N-C^{AF}, Fe-N-C-AW and Fe-N-C-Postpyr1. (b) Low magnification AC-HAADF STEM image of Fe$_{AD}$-N-C^{AF}. (c) Atomic resolution AC-HAADF STEM image of Fe$_{AD}$-N-C^{AF}, bright spots indicate atomically dispersed Fe sites. (d) AC-HAADF STEM image and corresponding EDS mapping of the Fe$_{AD}$-N-C^{AF} electrocatalyst.

In order to elucidate the transformations between the first and the second pyrolysis steps, XRD analysis was conducted also for Fe-N-C-Postpyr1. Analyzing the XRD spectrum of Fe-N-C-Postpyr1 and comparing it with that of Fe$_{AD}$-N-C^{AF} after the first and the second pyrolysis respectively, it is evident that the graphitic reflection at about 26° is less sharp after a single heat treatment highlighting that an additional pyrolysis step leads to enhanced graphitization. Iron/iron carbide clusters are visible at about 44.5° and 49°. The XRD pattern of Fe-N-C-AW still shows the presence of metallic nanoparticles after acid washing already observed for Fe_{AD}-N-C^{AF}, leading to the conclusion that graphitic carbon layers were able to protect those clusters from the dissolution in acid by encasing them [42].

The porous structure of Fe_{AD}-N-C^{AF} is confirmed by the low magnification aberration corrected high angle annular dark field (AC-HAADF) image in **Fig. 1 b**, which is in accord with SEM analysis in **Fig. S2**. The high mag AC-HAADF shown in **Fig. 1 c** demonstrates the presence of single bright points, which are atomically dispersed iron sites; however, some nanoparticles were observed as evident in **Fig. S1 c-d** and those results are in perfect agreement with the XRD pattern.

EDS further confirms the homogeneous dispersion of Fe atoms in the material and the effective doping of the carbonaceous structure with nitrogen moieties, as observed from elemental mapping in **Fig. 1 d**.

Raman spectra of Fe_{AD}-N-C^{AF} in **Fig. 2 a** is useful to evaluate the degree of disorder of carbon; the deconvolution is based on previous works present in literature [43,44], with the D1-band peak at 1360 cm^{-1} associated to defects in the graphene layers, the D3-band peak at about 1500 cm^{-1} related to amorphous carbon and its long-range disorder, the D4-band peak at about 1230 cm^{-1} assigned to the simultaneous presence of sp^2-sp^3 structures and finally the G-band peak at about 1580 cm^{-1} ascribed to sp^2 graphitic carbon. All the materials show similar trends as evident from **Fig. S3**, with values of intensity ratio I_D/I_G in the range of 1.05 to 1.09. This ratio is calculated based on the maximum values of the G and D bands and it is often reported in literature to quantify the relative amounts of ordered and disordered carbon. However, this value can lead to inaccurate conclusions when the broadening of the peaks is large as in this case and, as consequence, using the peak area is preferable. Based on this, all the samples show approximately two-thirds of carbon as disordered, demonstrating the presence of a large number of defects and a successful doping of the graphitic structure with nitrogen moieties already confirmed through EDS, which is beneficial for the reactions.

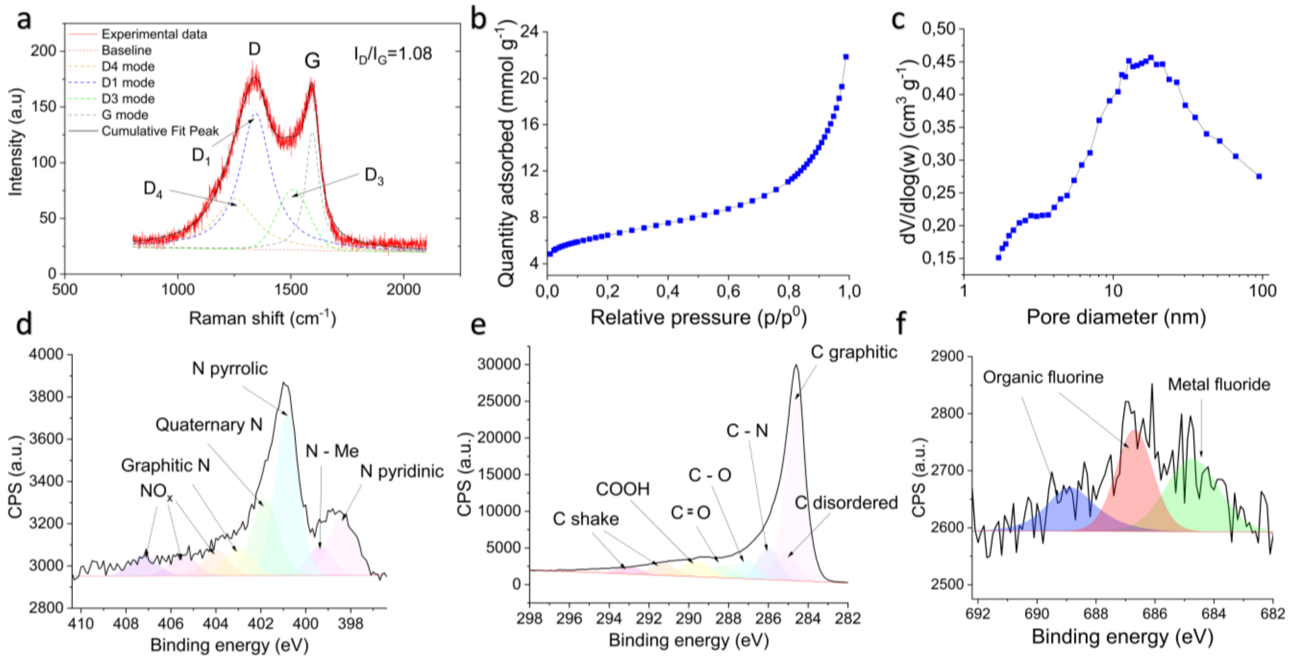

Figure 2. (a) Raman spectrum of Fe$_{AD}$-N-C^{AF}. (b) N_2 adsorption isotherm and (c) corresponding pore size distribution of Fe$_{AD}$-N-C^{AF}. (d-f) High-resolution N1s, C1s and F1s spectra respectively of Fe$_{AD}$-N-C^{AF}.

The BET analysis was conducted on Fe$_{AD}$-N-C^{AF} and Ni-N-C^{AF} samples and the results are presented in **Fig. 2 b-c** and **Fig. S4** respectively. Both the materials have almost the same specific surface area (482.9 m^2 g^{-1} and 477.2 m^2 g^{-1}, Ni and Fe electrocatalysts respectively) and pore size distribution, highlighting that the morphology of the material is dependent only on the choice of the silica templates. The hierarchical porous structure with mesopores and micropores is evident respectively from the distribution of the pore dimensions, with a broad peak centered at about 19 nm, and the adsorption isotherm, with a non-negligible uptake at the lowest values of relative pressure.

XPS spectra were used to analyze the surface chemical environment of the materials. High-resolution N1s, C1s and F1s spectra where deconvoluted based on previous studies [45–

50]. All the materials after the second pyrolysis have similar atomic composition as summarized in **Table 2**, with Fe_{AD}-N-C^{AF} showing the largest amount of nitrogen. The metal content is relatively low compared to previous works related to M-N-C electrocatalysts synthesized with the traditional sacrificial support method [51] and traces of silicon and fluorine coming from the silica templates and Teflon respectively are present.

Table 2. X-Ray photoelectron spectroscopy at. % concentration of Fe_{AD}-N-C^{AF}, Mn-N-C^{AF}, Co-N-C^{AF}, Ni-N-C^{AF} and Fe-N-C-Postpyr1.

Atomic %	**Fe-N-C-Postpyr1**	**Fe_{AD}-N-C^{AF}**	**Mn-N-C^{AF}**	**Ni-N-C^{AF}**	**Co-N-C^{AF}**
C 1s	90.47±0.35	94.86±0.47	94.39±1.53	93.54±1.55	96.19±0.49
N 1s	4.01±0.34	2.47±0.18	1.82±0.03	2.06±0.57	1.50±0.72
O 1s	4.58±0.52	2.58±0.28	3.65±1.44	4.20±2.04	2.01±0.98
Si 2p	0.30±0.03	0.07±0.01	0.09±0.06	0.04±0.01	0.11±0.06
Me 2p	0.04±0.04	0.01±0.00	0.02±0.02	0.10±0.01	0.03±0.03
F 1s	0.60±0.08	0.01±0.00	0.03±0.03	0.06±0.06	0.16±0.11

About nitrogen moieties in **Fig. 2 d**, the presence of N pyridinic at 398.2 eV, metal-nitrogen coordination at 399.4 eV, N pyrrolic at 400.8 eV, N quaternary at 401.8 eV, N graphitic at 402.9 eV and NO_x species respectively at 404.2 eV, 405.6 eV and 407.2 eV is observed. It is evident from **Tab. 3** that all the samples show a low ratio N pyridinic/N pyrrolic.

Table 3. X-Ray photoelectron spectroscopy high-resolution N 1s relative at. % concentration for Fe_{AD}-N-C^{AF}, Mn-N-C^{AF}, Co-N-C^{AF}, Ni-N-C^{AF} and Fe-N-C-Postpyr1.

N moiety	**Fe-N-C-Postpyr1**	**Fe_{AD}-N-C^{AF}**	**Mn-N-C^{AF}**	**Ni-N-C^{AF}**	**Co-N-C^{AF}**
N pyridinic	24.88±0.29	14.91±0.96	12.87±0.70	14.63±0.28	15.87±0.43
N-Me	13.78±0.81	6.62±2.45	6.45±0.36	7.57±0.35	6.36±0.57
N pyrrolic	31.65±2.83	35.71±0.24	38.99±1.31	33.78±2.35	36.27±0.86
N quaternary	11.89±1.59	19.19±0.91	14.78±0.36	18.24±1.42	17.20±1.11
N graphitic	6.95±0.46	7.17±0.82	9.89±1.29	9.52±0.68	9.25±1.57
NO_x	4.80±0.43	6.04±1.75	6.75±0.27	6.21±0.41	6.52±0.53
NO_x	3.90±0.16	5.29±1.01	5.08±0.89	4.76±0.74	4.24±0.68
NO_x	2.15±0.40	5.09±0.71	5.19±0.29	5.30±0.61	4.28±0.59

High-resolution carbon spectrum in **Fig. 2 e** shows graphitic carbon at 284.5 eV, disordered carbon at 285.1 eV, C-N bond at 286 eV, C-O at 287.1 eV, C=O at 288.3 eV, COOH at 289.7 eV, C-F_2 at 291.3 eV and C-F_3 at 293 eV. Graphitic carbon on the surface is predominant among carbon moieties as evident from **Table 4** and this is beneficial for corrosion resistance, while the presence of oxygenated species demonstrates an effective doping of graphene layers with defects [51]. C-F_2 and C-F_3 groups (C* shake) can be ascribed to the addition of Teflon to the precursors before the first pyrolysis step. High-resolution fluorine spectrum in **Fig. 2 f** obtained for the Fe_{AD}-N-C^{AF} sample show not only the presence of organic fluorine at binding energies greater than 686 eV but also the formation of metal fluoride species at 685 eV.

Table 4. X-Ray photoelectron spectroscopy high-resolution C 1s relative at. % concentration for Fe_{AD}-N-C^{AF}, Mn-N-C^{AF}, Co-N-C^{AF}, Ni-N-C^{AF} and Fe-N-C-Postpyr1.

C moiety	**Fe-N-C-Postpyr1**	**Fe_{AD}-N-C^{AF}**	**Mn-N-C^{AF}**	**Ni-N-C^{AF}**	**Co-N-C^{AF}**
C graphitic	51.97±4.05	54.30±1.69	48.49±6.03	46.46±4.56	58.57±0.55
C disordered	14.45±4.36	9.31±1.48	14.63±5.07	15.52±4.23	5.62±0.34
C-N	10.55±1.34	10.54±0.42	11.59±2.08	13.57±2.12	9.59±0.47
C-O	6.87±0.43	6.36±0.23	6.35±0.82	5.86±0.76	6.04±0.48
C=O	4.30±0.76	4.64±0.01	4.13±0.68	4.11±0.94	4.64±0.19
COOH	6.03±0.40	7.18±0.22	7.78±1.37	8.24±1.22	7.08±0.19
C shake*	3.57±0.54	4.73±0.09	4.18±0.59	3.91±0.86	5.23±0.17
C shake*	2.26±0.52	2.96±0.10	2.44±0.47	2.31±0.67	3.24±0.08

Table 1 also highlights how elemental composition significantly varies between Fe-N-C-Postpyr1 and Fe_{AD}-N-C^{AF}, with the former showing larger amounts of nitrogen and oxygen atoms that during the second pyrolysis were partially removed forming gaseous products. Interestingly, non-negligible amounts of silicon and fluorine are still present in the Fe-N-C-Posypyr1 sample and this is evidence of the fact that a second heat treatment is necessary to reduce their content to negligible values. The largest differences in the nitrogen moieties are a significantly greater ratio N pyridinic/N pyrrolic and approximately a double amount of nitrogen coordinated to iron in Fe-N-C-Postpyr1, while high-resolution carbon spectra demonstrate that a second heat treatment enhances graphitization by exposing carbon to high temperature for additional time and this is in line with XRD analysis. Additional XPS images for the other samples can be found in **Fig. S5**.

3.2 Electrochemical study on RRDE

Higher values of E_{onset} and $E_{1/2}$ are indicators of enhanced electrocatalytic activity, since a lower overpotential to achieve a determined value of current density is necessary. $\%H_2O_2$ and n are useful to understand the reaction mechanism and they are dependent on each other. In particular, a value of n equal to 4 means that $4e^{-}$ pathway is realized and this correspond to the absence of hydrogen peroxide generation which is beneficial for performances. Since they are dependent on the applied potential, their averages in the potential window from 0.25 V to E_{onset} are also reported for convenience in this study.

Fig. S6 shows the ORR polarization curves and the ring currents of Fe_{AD}-N-C^{AF}, Mn-N-C^{AF}, Co-N-C^{AF} and Ni-N-C^{AF} electrocatalysts in 0.1 M $HClO_4$, 0.1 M KOH, 0.5 M NaCl and 2 M NaCl respectively with an electrocatalyst loading of 0.6 mg cm^{-2} at 1600 rpm, where commercial Pt/C is used as reference with a loading of 60 μg cm^{-2}. Additionally, the trends of n and % H_2O_2 as function of the applied potential are reported in **Fig. S7**.

As expected from previous works [52], Fe_{AD}-N-C^{AF} electrocatalyst show better performances among PGM-free materials because of its intrinsic higher electrocatalytic property and the general trend of activity is Fe_{AD}-N-C^{AF} > Mn-N-C^{AF} > Co-N-C^{AF} > Ni-N-C^{AF} in every type of electrolyte, as demonstrated in **Fig. 3 a-b** in terms of $E_{1/2}$ and E_{onset}. In detail, as shown in **Tab. S2**, halfwave potentials of 0.81 V in alkaline environment (0.82 V with Pt/C) and 0.70 V in acidic solution were achieved with Fe_{AD}-N-C^{AF}. Higher activities are reached in alkaline electrolyte and this is in line with the fact that ORR is kinetically favored in this kind of medium because of improved charge transfer [53]. Poor performance is evident, also from **Table S3**, in both neutral solutions since the scarcity of protons H^{+} and hydroxyl ions OH^{-} is a limiting factor.

The iron-based electrocatalyst also presents almost a $4e^{-}$ pathway in 0.1 M $HClO_4$, 0.1 M KOH, 0.5 M NaCl with negligible H_2O_2 production, as highlighted in **Fig. 3 c-d**, while all the materials present a sharp reduction of *n* in neutral solution when increasing NaCl concentration from 0.5 M to 2 M.

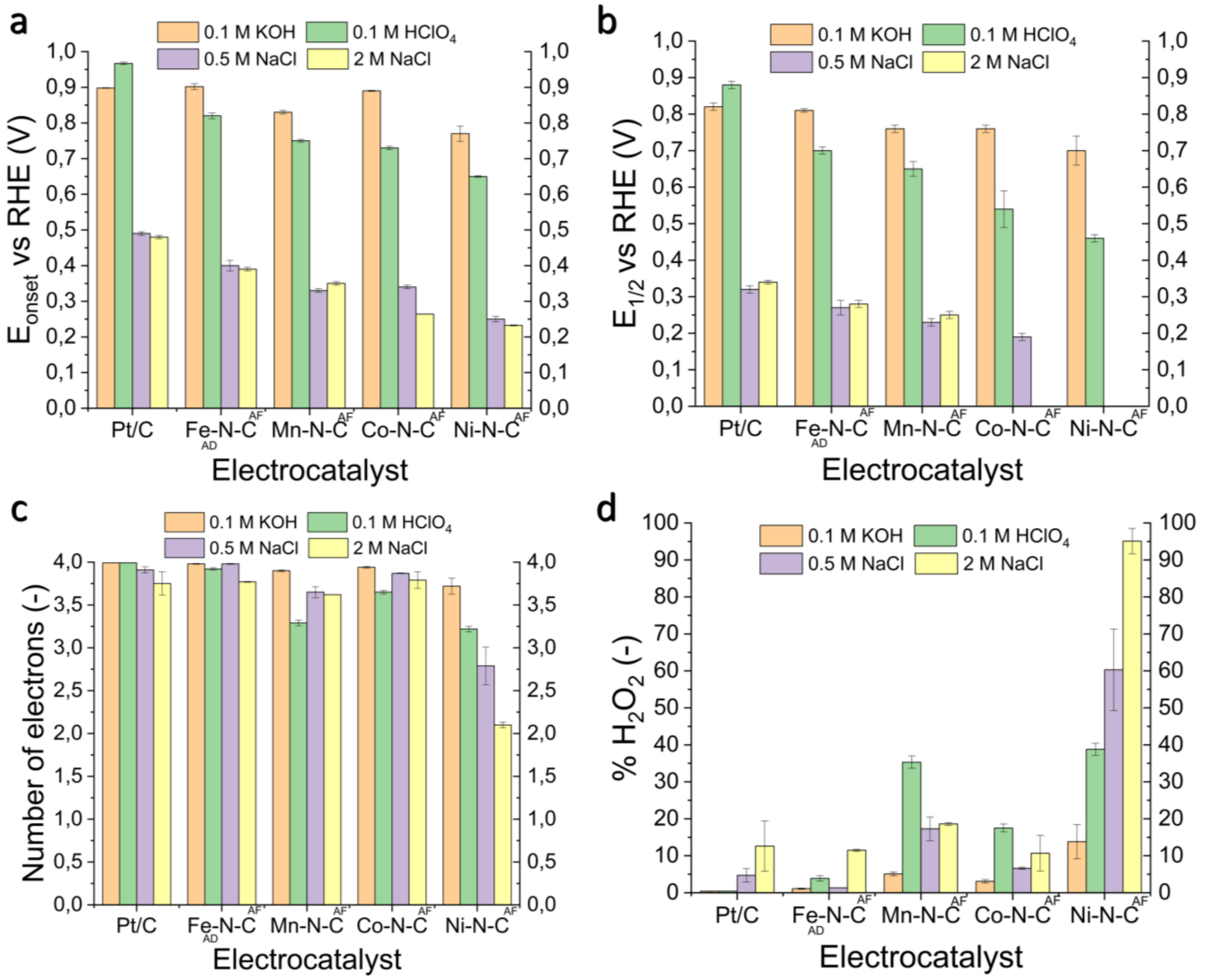

Figure 3. Electrochemical performance on RRDE. (a) E_{onset}, (b) $E_{1/2}$, (c) number of transferred electrons n and (d) %H_2O_2 of M-N-C electrocatalysts and Pt/C in 4 different electrolytes.

The following discussion is focused only on the acid medium since the gap with platinum is still strong in this kind of environment. Fe_{AD}-N-C^{AF} ORR activity was further compared in acid electrolyte with Fe-N-C-Postpyr1, Fe-N-C-AW, Fe_{AD}-N-C^{AF}-BM. As clear from **Fig. 4**, the second pyrolysis step leads to a strong enhancement of activity highlighting that after only a single heat treatment the configurations of carbon and nitrogen together with relatively high surface contents of silicon and fluorine result in a reasonably lower active site density. As expected, the acid-washing did not cause any change in the final performance since no phase transformations were observed while an additional ball-milling step led to a 20 mV positive shift of the halfwave potential, as result of greater homogeneity of particle size distribution.

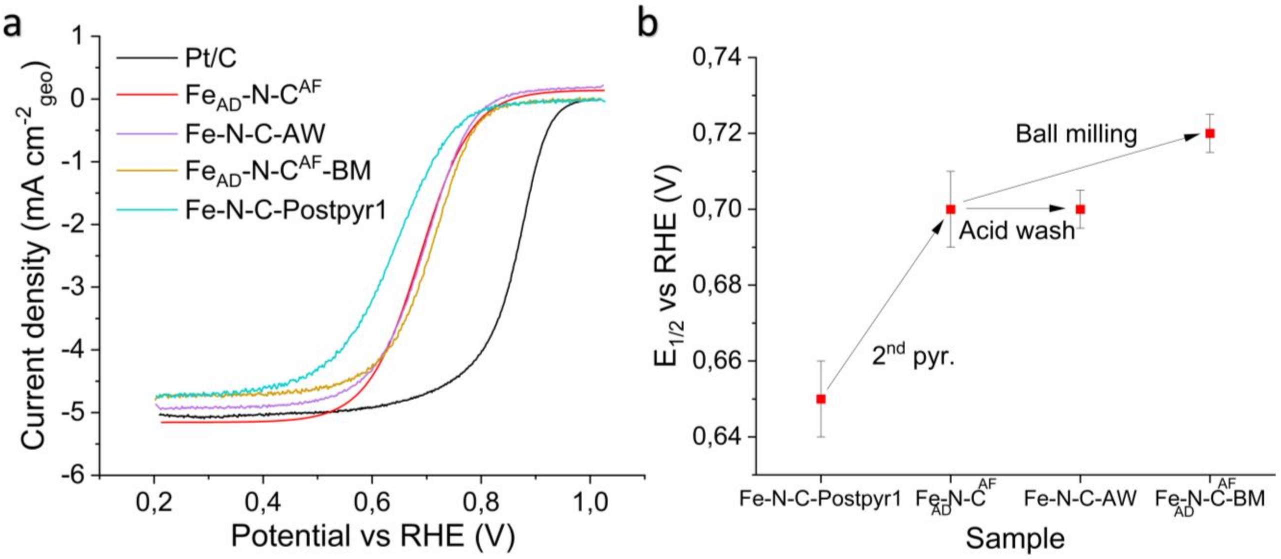

Figure 4. (a) ORR polarization curves and (b) variation of $E_{1/2}$ of the iron-based electrocatalyst at different synthetic steps in 0.1 M $HClO_4$ at 1600 rpm with a loading of 600 μg cm^{-2}.

Those results demonstrate that the acid-free method based on the use of Teflon can be a successful variation of the traditional SSM to synthesize materials for ORR electrocatalysis, with activity comparable to state-of-the-art non-precious electrocatalysts as shown in **Table S5**. For the sake of comparison, the iron-based material show slightly lower performances in alkaline medium respect to Fe-N-C-like electrocatalysts synthesized by traditional sacrificial support method with 25 wt. % HF, also using nicarbazin as source of carbon and nitrogen atoms [51]. This further confirms the goodness of this novel synthesis approach, which is still all to be optimized.

Additionally, a study on the electrocatalyst loading from 50 μg cm^{-2} to 900 μg cm^{-2} was conducted for the Fe$_{AD}$-N-C^{AF}-BM sample, the one showing the highest activity in acid medium. In this way it is possible to obtain precious information about the real reaction mechanism. **Fig. 5 a-b** show how halfwave potential and hydrogen peroxide yield respectively change by varying the electrocatalyst loading, pointing out that the performance reaches a plateau at 700 μg cm^{-2} with a value of $E_{1/2}$ of 0.73 V. Increasing the loading does not lead to a proportional increase of activity since, when the thickness of the electrocatalytic layer is relatively large on the disk, oxygen is not able to easily reach all the active sites of the material because of mass transfer limitations.

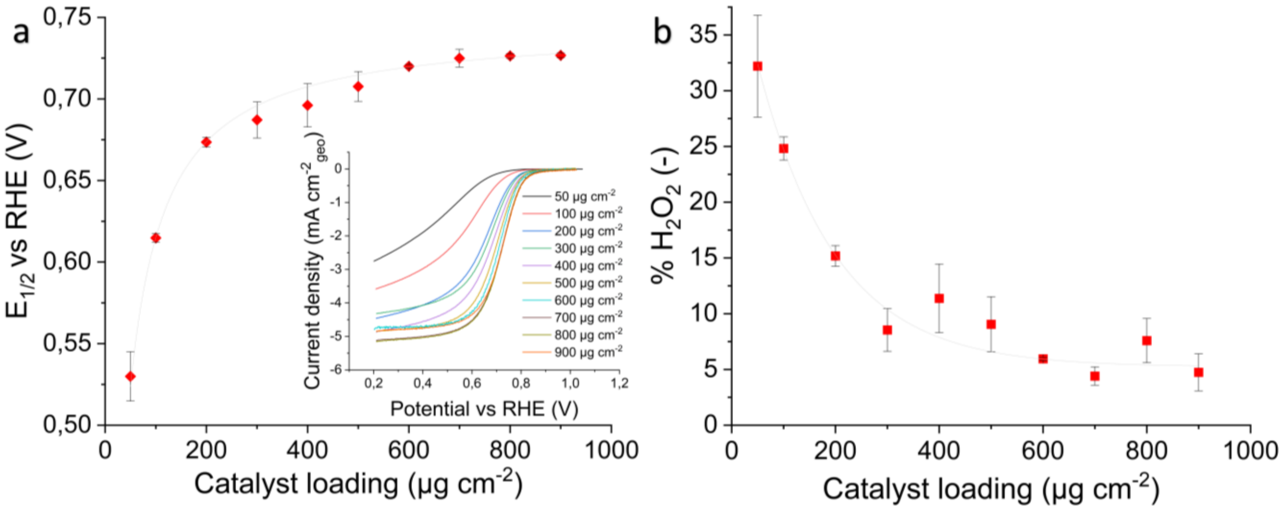

Figure 5. (a) $E_{1/2}$ with corresponding polarization curves and (b) %H_2O_2 of Fe$_{AD}$-N-C^{AF}-BM in 0.1 M $HClO_4$ at 1600 rpm with electrocatalyst loading varying from 50 μg cm^{-2} to 900 μg cm^{-2}.

In the range of 50 μg cm^{-2} to 300 μg cm^{-2}, hydrogen peroxide yield has a sharp reduction and this reveals a 2x2e^{-} pathway; in particular, when the loading increases, H_2O_2 has a greater probability of being further reduced to H_2O inside the material before reaching the ring and it is not detected as ring current.

Accelerated durability testing was conducted on Fe_{AD}-N-C^{AF}-BM in acid medium through cycling in the typical potential window of operation in systems such as PEMFCs. It is well known that while the activity of PGM-free electrocatalysts has made promising improvements, the stability of those materials in acid medium is distant from technical requirements for their commercialization. Issues such as demetallation, flooding of micropores and carbon corrosion lead to a fast degradation of performances after few hours [6].

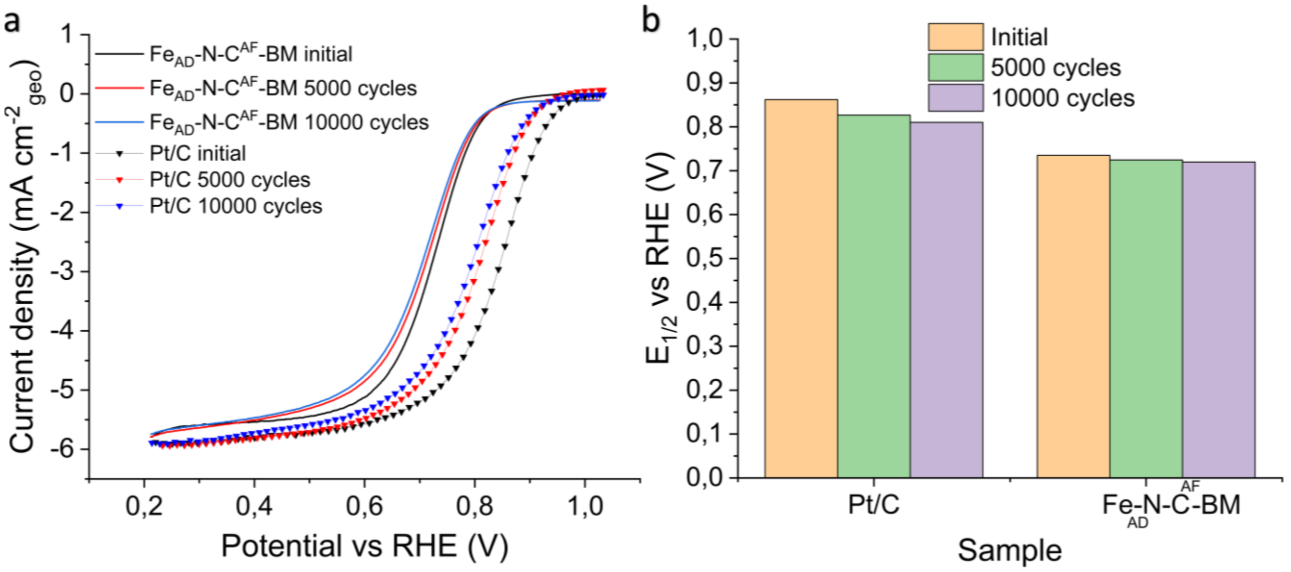

Figure 6. Accelerated durability test on RRDE conducted on Fe_{AD}-N-C^{AF}-BM with a loading of 700 µg cm^{-2} and Pt/C with a loading of 60 µg cm^{-2} in 0.1 M $HClO_4$ at 1600 rpm. (a) ORR polarization curves and (b) $E_{1/2}$ before and after potential cycling.

Fig. 6 a-b demonstrate excellent stability on RRDE of Fe_{AD}-N-C^{AF}-BM with a reduction of $E_{1/2}$ of 1.4% (4.1% for Pt/C) and 2.1% (6.0% for Pt/C) after 5000 and 10000 cycles respectively respect to the initial value, with negligible variation of the average number of transferred electrons. This result further confirms that this novel synthesis method could be a successful way to synthesize non-precious materials with enhanced electrocatalytic properties and stability, that can be reasonably ascribed to the presence of a hierarchical porous structure successfully doped with active sites and with a high degree of surface graphitization, as verified through physical-chemical characterization.

4. Conclusions and future perspectives

In summary, a novel and sustainable process for the synthesis of electrocatalysts with atomically dispersed active sites was presented in this study. In particular, it was demonstrated that the iron-based material shows activity towards ORR comparable to state-of-the-art PGM-free electrocatalysts with excellent stability in acid medium. This unique approach to synthesize non-precious materials is all to be explored also for different electrocatalytic processes, with the possibility to finely tune the tridimensional structure and porosity of the electrocatalyst by varying synthesis conditions, precursors and mass ratios, silica templates and morphology of polytetrafluoroethylene powder.

CRediT authorship Contribution statement

Alessio Cosenza: Methodology, Investigation, Formal analysis, Writing – Original draft; **Laurent Delafontaine**: Methodology, Investigation; **Alvin Ly**: Methodology; **Hanson Wang**: Methodology; **Eamonn Murphy**: Methodology; **Yuanchao Liu**: Methodology; **Stefania Specchia**: Supervision, Formal analysis, Writing – Review & Editing; **Plamen Atanassov**: Supervision, Formal analysis, Writing – Review & Editing, Funding acquisition, Resources.

Declaration of Competing Interest

The authors declare that they have no known competing financial interests or personal relationships that could have appeared to influence the work reported in this paper.

Data availability

Data will be made available on request.

Acknowledgements

This work was supported financially by the Advanced Photon Source [grant number DE-AC02-06CH11357]; National Science Foundation Major Research Instrumentation Program [grant number CHE-1338173]; A.C. acknowledges the Erasmus+ grant n. 2020-1-IT02-KA107-078119 for supporting his stay at UCI in 2022; S.S. acknowledges the funding provided by the Staff Mobility for Training Activities between programme and partner countries within the Program Erasmus+/KA1 Call 2019 (International Credit Mobility, year 2020/2021) for visiting UCI in 2022. The authors would like to acknowledge Dr. Jose Eduardo Ortega Aguilar and Dr. See Wee Chee for help with the TEM imaging and EDS mapping.

References

[1] N.B. Grimm, F.S. Chapin, B. Bierwagen, P. Gonzalez, P.M. Groffman, Y. Luo, F. Melton, K. Nadelhoffer, A. Pairis, P.A. Raymond, J. Schimel, C.E. Williamson, The impacts of climate change on ecosystem structure and function, Front. Ecol. Environ. 11 (2013) 474–482. https://doi.org/10.1890/120282.

[2] P. Challa, G. Paleti, V.R. Madduluri, S.B. Gadamani, R. Pothu, D.R. Burri, R. Boddula, V. Perugopu, S.R.R. Kamaraju, Trends in Emission and Utilization of CO_2: Sustainable Feedstock in the Synthesis of Value-Added Fine Chemicals, Catal. Surv. Asia. 26 (2022) 80–91. https://doi.org/10.1007/s10563-021-09352-6.

[3] Y. Wang, R. Yi, A. Chen, C. Fang, Y. Wang, Q. Yi, M. Liu, S. Liu, S. Zhan, B. Zhong, Hollow Carbon Sphere and Polyhedral Carbon Composites Supported Iron Nanoparticles as Excellent Bifunctional Electrocatalysts of Zn–Air Battery, Energy Technol. 10 (2022) 2200057. https://doi.org/10.1002/ente.202200057.

[4] PGM management, Matthey.Com. (n.d.). https://matthey.com/products-and-markets/pgms-and-circularity/pgm-management (accessed July 22, 2022).

[5] J. Zhang, ed., PEM Fuel Cell Electrocatalysts and Catalyst Layers, Springer London, London, 2008. https://doi.org/10.1007/978-1-84800-936-3.

[6] L. Ding, T. Tang, J.-S. Hu, Recent Progress in Proton-Exchange Membrane Fuel Cells Based on Metal-Nitrogen-Carbon Catalysts, Acta Phys. Chim. Sin. 37 (2020) 2010048. https://doi.org/10.3866/PKU.WHXB202010048.

[7] S. Stariha, K. Artyushkova, M.J. Workman, A. Serov, S. Mckinney, B. Halevi, P. Atanassov, PGM-free Fe-N-C catalysts for oxygen reduction reaction: Catalyst layer design, J. Power Sources. 326 (2016) 43–49. https://doi.org/10.1016/j.jpowsour.2016.06.098.

[8] R. Jasinski, A new fuel cell cathode catalyst, Nature. 201 (1964) 1212–1213. https://doi.org/10.1038/2011212a0.

[9] Y. He, Q. Tan, L. Lu, J. Sokolowski, G. Wu, Metal-Nitrogen-Carbon Catalysts for Oxygen Reduction in PEM Fuel Cells: Self-Template Synthesis Approach to Enhancing Catalytic Activity and Stability, Electrochem. Energy Rev. 2 (2019) 231–251. https://doi.org/10.1007/s41918-019-00031-9.

[10] J.H. Zagal, S. Specchia, P. Atanassov, Mapping transition metal-MN_4 macrocyclic complex catalysts performance for the critical reactivity descriptors, Curr. Opin. Electrochem. 27 (2021) 100683. https://doi.org/10.1016/j.coelec.2020.100683.

[11] T. Asset, P. Atanassov, Iron-Nitrogen-Carbon Catalysts for Proton Exchange Membrane Fuel Cells, Joule. 4 (2020) 33–44. https://doi.org/10.1016/j.joule.2019.12.002.

[12] J. Liu, Z. Jin, X. Wang, J. Ge, C. Liu, W. Xing, Recent advances in active sites identification and regulation of M-N/C electro-catalysts towards ORR, Sci. China Chem. 62 (2019) 669–683. https://doi.org/10.1007/s11426-018-9425-5.

[13] S. Specchia, P. Atanassov, J.H. Zagal, Mapping transition metal–nitrogen–carbon catalyst performance on the critical descriptor diagram, Curr. Opin. Electrochem. 27 (2021) 100687. https://doi.org/10.1016/j.coelec.2020.100687.

[14] M. Rauf, Y.-D. Zhao, Y.-C. Wang, Y.-P. Zheng, C. Chen, X.-D. Yang, Z.-Y. Zhou, S.-G. Sun, Insight into the different ORR catalytic activity of Fe/N/C between acidic and alkaline media: Protonation of pyridinic nitrogen, Electrochem. Commun. 73 (2016) 71–74. https://doi.org/10.1016/j.elecom.2016.10.016.

[15] K.H. Lim, H. Kim, Nitrogen-doped carbon catalysts derived from ionic liquids in the presence of transition metals for the oxygen reduction reaction, Appl. Catal. B Environ. 158–159 (2014) 355–360. https://doi.org/10.1016/j.apcatb.2014.04.038.

[16] L. Osmieri, Transition Metal–Nitrogen–Carbon (M–N–C) Catalysts for Oxygen Reduction Reaction. Insights on Synthesis and Performance in Polymer Electrolyte Fuel Cells, ChemEngineering. 3 (2019) 16. https://doi.org/10.3390/chemengineering3010016.

[17] L. Osmieri, L. Pezzolato, S. Specchia, Recent trends on the application of PGM-free catalysts at the cathode of anion exchange membrane fuel cells, Curr. Opin. Electrochem. 9 (2018) 240–256. https://doi.org/10.1016/j.coelec.2018.05.011.

[18] G. Long, K. Wan, M. Liu, X. Li, Z. Liang, J. Piao, Effect of pyrolysis conditions on nitrogen-doped ordered mesoporous carbon electrocatalysts, Chin. J. Catal. 36 (2015) 1197–1204. https://doi.org/10.1016/S1872-2067(15)60912-3.

[19] Y. Huang, Y. Chen, M. Xu, T. Asset, P. Tieu, A. Gili, D. Kulkarni, V. De Andrade, F. De Carlo, H.S. Barnard, A. Doran, D.Y. Parkinson, X. Pan, P. Atanassov, I.V. Zenyuk, Catalysts by pyrolysis: Direct observation of chemical and morphological transformations leading to transition metal-nitrogen-carbon materials, Mater. Today. 47 (2021) 53–68. https://doi.org/10.1016/j.mattod.2021.02.006.

[20] C. Domínguez, M.A. Peña, S. Rojas, F.J. Pérez-Alonso, Effect of the pyrolysis atmosphere and nature of iron precursor on the structure and activity of Fe/N based electrocatalysts for the oxygen reduction reaction, Int. J. Hydrog. Energy. 41 (2016) 22560–22569. https://doi.org/10.1016/j.ijhydene.2016.08.191.

[21] L. Osmieri, A.H.A. Monteverde Videla, S. Specchia, Activity of Co–N multi walled carbon nanotubes electrocatalysts for oxygen reduction reaction in acid conditions, J. Power Sources. 278 (2015) 296–307. https://doi.org/10.1016/j.jpowsour.2014.12.080.

[22] F.J. Pérez-Alonso, M.A. Salam, T. Herranz, J.L. Gómez de la Fuente, S.A. Al-Thabaiti, S.N. Basahel, M.A. Peña, J.L.G. Fierro, S. Rojas, Effect of carbon nanotube diameter for the synthesis of Fe/N/multiwall carbon nanotubes and repercussions for the oxygen reduction reaction, J. Power Sources. 240 (2013) 494–502. https://doi.org/10.1016/j.jpowsour.2013.04.086.

[23] N. Wang, M. Zhang, L. Liu, J. Zheng, J. Xu, T. Hayat, N.S. Alharbi, Space-confined pyrolysis for fabrication of peacods-like Fe_3O_4@C-Ni nanostructures for catalysis and protein adsorption, Nanotechnology. 30 (2019) 415602. https://doi.org/10.1088/1361-6528/ab2ff0.

[24] A. Serov, K. Artyushkova, P. Atanassov, Fe-N-C oxygen reduction fuel cell catalyst derived from carbendazim: synthesis, structure, and reactivity, Adv. Energy Mater. 4 (2014) 1301735. https://doi.org/10.1002/aenm.201301735.

[25] A.H.A. Monteverde Videla, L. Osmieri, M. Armandi, S. Specchia, Varying the morphology of Fe-N-C electrocatalysts by templating Iron Phthalocyanine precursor with different porous SiO_2 to promote the Oxygen Reduction Reaction, Electrochimica Acta. 177 (2015) 43–50. https://doi.org/10.1016/j.electacta.2015.01.165.

[26] J.M. Ziegelbauer, T.S. Olson, S. Pylypenko, F. Alamgir, C. Jaye, P. Atanassov, S. Mukerjee, Direct Spectroscopic Observation of the Structural Origin of Peroxide Generation from Co-Based Pyrolyzed Porphyrins for ORR Applications, J. Phys. Chem. C. 112 (2008) 8839–8849. https://doi.org/10.1021/jp8001564.

[27] L. Osmieri, A.H.A. Monteverde Videla, M. Armandi, S. Specchia, Influence of different transition metals on the properties of Me–N–C (Me = Fe, Co, Cu, Zn) catalysts synthesized using SBA-15 as tubular nano-silica reactor for oxygen reduction reaction, Int. J. Hydrog. Energy. 41 (2016) 22570–22588. https://doi.org/10.1016/j.ijhydene.2016.05.223.

[28] H.-S. Oh, J.-G. Oh, B. Roh, I. Hwang, H. Kim, Development of highly active and stable non-precious oxygen reduction catalysts for PEM fuel cells using polypyrrole and a chelating agent, Electrochem. Commun. 13 (2011) 879–881. https://doi.org/10.1016/j.elecom.2011.05.027.

[29] T. Asset, F. Maillard, F. Jaouen, Electrocatalysis with Single-Metal Atom Sites in Doped Carbon Matrices, in: P. Serp, D.P. Minh (Eds.), Support. Met. Single At. Catal., 1st ed., Wiley, 2022: pp. 531–582. https://doi.org/10.1002/9783527830169.ch13.

[30] G. Wu, C.M. Johnston, N.H. Mack, K. Artyushkova, M. Ferrandon, M. Nelson, J.S. Lezama-Pacheco, S.D. Conradson, K.L. More, D.J. Myers, Synthesis–structure–performance correlation for polyaniline–Me–C non-precious metal cathode catalysts for oxygen reduction in fuel cells, J. Mater. Chem. 21 (2011) 11392–11405. https://doi.org/10.1039/C0JM03613G.

[31] Pajarito Powder, (n.d.). https://pajaritopowder.com/ (accessed July 22, 2022).

[32] D.K. Singh, K.S. Krishna, S. Harish, S. Sampath, M. Eswaramoorthy, No more HF: teflon-assisted ultrafast removal of silica to generate high-surface-area mesostructured carbon for enhanced CO_2 capture and supercapacitor performance, Angew. Chem. Int. Ed. 55 (2016) 2032–2036. https://doi.org/10.1002/anie.201509054.

[33] Y. Liang, Q. Cao, M. Zheng, H. Huo, H. Hu, H. Dong, Y. Xiao, Y. Liu, Teflon: A decisive additive in directly fabricating hierarchical porous carbon with network structure

from natural leaf, ACS Sustain. Chem. Eng. 5 (2017) 9307–9312. https://doi.org/10.1021/acssuschemeng.7b02318.

[34] W. Teng, Y. Zhong, R. Liu, Synthesis of ordered mesoporous carbons by Teflon-assisted removal of silica template in tri-constituent co-assembly for supercapacitors, Emergent Mater. 3 (2020) 339–346. https://doi.org/10.1007/s42247-020-00087-0.

[35] A.I. Stankiewicz, P. Yan, 110th anniversary: the missing link unearthed: materials and process intensification, Ind. Eng. Chem. Res. 58 (2019) 9212–9222.

[36] T. Van Gerven, A. Stankiewicz, Structure, energy, synergy, time: The fundamentals of process intensification, Ind. Eng. Chem. Res. 48 (2009) 2465–2474.

[37] W. Stöber, A. Fink, E. Bohn, Controlled growth of monodisperse silica spheres in the micron size range, J. Colloid Interface Sci. 26 (1968) 62–69. https://doi.org/10.1016/0021-9797(68)90272-5.

[38] A. Bonakdarpour, T.R. Dahn, R.T. Atanasoski, M.K. Debe, J.R. Dahn, H_2O_2 Release during Oxygen Reduction Reaction on Pt Nanoparticles, (n.d.) 4.

[39] R. Zhou, Y. Zheng, M. Jaroniec, S.-Z. Qiao, Determination of the electron transfer number for the oxygen reduction reaction: from theory to experiment, Acs Catal. 6 (2016) 4720–4728. https://doi.org/10.1021/acscatal.6b01581.

[40] E. Thompson, A. Danks, L. Bourgeois, Z. Schnepp, Iron-catalyzed graphitization of biomass, Green Chem. 17 (2015) 551–556. https://doi.org/10.1039/c4gc01673d.

[41] C. Chen, K. Sun, A. Wang, S. Wang, J. Jiang, Catalytic graphitization of cellulose using nickel as catalyst, BioResources. 13 (2018) 3165–3176. https://doi.org/10.15376/biores.13.2.3165-3176.

[42] Y. Hu, J.O. Jensen, W. Zhang, L.N. Cleemann, W. Xing, N.J. Bjerrum, Q. Li, Hollow Spheres of Iron Carbide Nanoparticles Encased in Graphitic Layers as Oxygen Reduction Catalysts, Angew. Chem. Int. Ed. 53 (2014) 3675–3679. https://doi.org/10.1002/anie.201400358.

[43] A. Ramya, A.N. Mohan, B. Manoj, Wrinkled graphene: synthesis and characterization of few layer graphene-like nanocarbons from kerosene, Mater. Sci.-Pol. 34 (2016) 330–336. https://doi.org/10.1515/msp-2016-0061.

[44] S.A. Pfau, A. La Rocca, E. Haffner-Staton, G.A. Rance, M.W. Fay, R.J. Brough, S. Malizia, Comparative nanostructure analysis of gasoline turbocharged direct injection and diesel soot-in-oil with carbon black, Carbon. 139 (2018) 342–352. https://doi.org/10.1016/j.carbon.2018.06.050.

[45] S. Kabir, K. Artyushkova, A. Serov, B. Kiefer, P. Atanassov, Binding energy shifts for nitrogen-containing graphene-based electrocatalysts–experiments and DFT calculations, Surf. Interface Anal. 48 (2016) 293–300. https://doi.org/10.1002/sia.5935.

[46] R. Gokhale, Y. Chen, A. Serov, K. Artyushkova, P. Atanassov, Direct synthesis of platinum group metal-free Fe-NC catalyst for oxygen reduction reaction in alkaline media, Electrochem. Commun. 72 (2016) 140–143. https://doi.org/10.1016/j.elecom.2016.09.013.

[47] M.N. Hossain, J. Wen, A. Chen, Unique copper and reduced graphene oxide nanocomposite toward the efficient electrochemical reduction of carbon dioxide, Sci. Rep. 7 (2017) 1–10. https://doi.org/10.1038/s41598-017-03601-3.

[48] C. Zhang, Q. Jintao, K. Fei, H. Xingmin, F. Zhi, Y. Yu, S. Tao, Plasma surface treatment of Cu by nanosecond-pulse diffuse discharges in atmospheric air, Plasma Sci. Technol. 20 (2017) 014011. https://doi.org/10.1088/2058-6272/aa8c6e.

[49] J. Ebner, D. McFadden, R. Walton, The x-ray photoelectron spectra of inorganic molecules. XI1. Fluorine 1s binding energies in metal fluorides, J. Solid State Chem. 17 (1976) 447–449. https://doi.org/10.1016/S0022-4596(76)80016-3.

[50] U.S. Waware, A. Hamouda, M. Rashid, P. Kasak, Binding energy, structural, and dielectric properties of thin film of poly (aniline-co-m-fluoroaniline), Ionics. 24 (2018) 3249–3257. https://doi.org/10.1007/s11581-018-2516-4.

[51] M.M. Hossen, K. Artyushkova, P. Atanassov, A. Serov, Synthesis and characterization of high performing Fe-NC catalyst for oxygen reduction reaction (ORR) in Alkaline Exchange Membrane Fuel Cells, J. Power Sources. 375 (2018) 214–221. https://doi.org/10.1016/j.jpowsour.2017.08.036.

[52] H. Xu, D. Wang, P. Yang, A. Liu, R. Li, Y. Li, L. Xiao, X. Ren, J. Zhang, M. An, Atomically dispersed M–N–C catalysts for the oxygen reduction reaction, J. Mater. Chem. A. 8 (2020) 23187–23201. https://doi.org/10.1039/d0ta08732g.

[53] K.I. Ozoemena, Nanostructured platinum-free electrocatalysts in alkaline direct alcohol fuel cells: catalyst design, principles and applications, RSC Adv. 6 (2016) 89523–89550. https://doi.org/10.1039/C6RA15057H.